The Response of an Inerter-Based Dynamic Vibration Absorber With a Parametrically Excited Centrifugal Pendulum

Aakash Gupta
Department of Mechanical Engineering,
Michigan State University,
East Lansing, MI 48824
e-mail: guptaaa3@msu.edu

Wei-Che Tai
Department of Mechanical Engineering,
Michigan State University,
East Lansing, MI 48824
e-mail: taiweich@msu.edu

The inerter has been integrated into various vibration mitigation devices, whose mass amplification effect could enhance the suppression capabilities of these devices. In the current study, the inerter is integrated with a pendulum vibration absorber, referred to as inerter pendulum vibration absorber (IPVA). To demonstrate its efficacy, the IPVA is integrated with a linear, harmonically forced oscillator seeking vibration mitigation. A theoretical investigation is conducted to understand the nonlinear response of the IPVA. It is shown that the IPVA operates based on a nonlinear energy transfer phenomenon wherein the energy of the linear oscillator transfers to the pendulum vibration absorber as a result of parametric resonance of the pendulum. The parametric instability is predicted by the harmonic balance method along with the Floquet theory. A perturbation analysis shows that a pitchfork bifurcation and period doubling bifurcation are necessary and sufficient conditions for the parametric resonance to occur. An arc-length continuation scheme is used to predict the boundary of parametric instability in the parameter space and verify the perturbation analysis. The effects of various system parameters on the parametric instability are examined. Finally, the IPVA is compared with a linear benchmark and an autoparametric vibration absorber and shows more efficacious vibration suppression.
[DOI: 10.1115/1.4053789]

Keywords: dynamics, nonlinear vibration, vibration control

1 Introduction

The inerter is a mechanical device with two terminals, each of which exerts an equal and opposite inertial force proportional to the relative acceleration between the terminals [1]. The inerter amplifies the inertial effects of a small mass by using motion transmission mechanisms, fluids, and levers [1]. By virtue of its mass amplification effect, the inerter has been studied to improve the performance of various passive vibration mitigation techniques in the last decade. Ikago et al. [2] developed the tuned viscous mass damper (TVMD), which consisted of a tuning spring in series with the inerter and a viscous damper in parallel. It was shown that the TVMD outperformed the viscous damper alone when applied to a seismically excited single degree-of-freedom (SDOF) structure. Furthermore, Lazar et al. [3] proposed the tuned inerter damper (TID), wherein the inerter was substituted for the oscillating mass of a tuned mass damper (TMD). The TID and TMD were compared in seismically excited multiple-degree-of-freedom structures and demonstrated similar effectiveness. Later, Lazar et al. [4] considered the TID in suppressing the midspan vibration of cables and showed that the TID outperformed the optimal viscous damper. Moreover, Qian et al. [5] studied serial and parallel connections between the TID and a base-isolation system and concluded that the serial TID outperformed the parallel TID for practical structures.

The inerter has also been applied to enhance the inertial effects of dynamic vibration absorbers (DVAs). Marian and Giaralis [6] proposed the tuned mass damper inerter (TMDI), which consisted of a TMD and the inerter in series. In a 3DOF structure simulation, they showed that for achieving similar vibration control performance, the

weight of the TMDI was four times lighter than the TMD. Furthermore, De Domenico and Ricciardi [7] incorporated the TMDI in a base-isolation system and demonstrated that the displacement demand of the base-isolated structure could be significantly reduced. Moreover, Joubaneh and Barry [8] studied the performance of four models of electromagnetic resonant shunt TMDI (ERS-TMDI) on both vibration suppression and energy harvesting and identified the best model. Their parametric studies showed that increasing the inertance enhances the performance of the best model in terms of both vibration mitigation and energy harvesting. On the other hand, Tai [9] proposed the tuned inerter-torsional-mass damper (TITMD), which integrated the inerter and a torsional mass damper. In comparison with the TMDI, the TITMD achieved 20–70% improvement when having identical weights.

In recent years, the inerter has been integrated with nonlinear vibration absorbers. Qian and Zuo [10] considered the effects of adding an inerter to a nonlinear vibration absorber. The nonlinear vibration absorber consisted of a tuned mass damper with nonlinear spring containing both linear and cubic stiffness. They observed that the spring-inerter-damper system added to the beam outperformed the nonlinear vibration absorber without inerter. Furthermore, Kakou and Barry [11] added a nonlinear spring to the electromagnetic resonant shunt tuned mass damper-inerters (ERS-TMDI) [8] to analyze the implications of coupling a nonlinear spring to the system. Two configurations of the system, one with the energy harvester between the tuned mass and ground and other with the energy harvester between primary structure mass and the tuned mass, were compared for their efficacy in vibration suppression and energy harvesting of the system. It was found that Configuration-1 exhibits higher range of feasible forcing without degrading the performance compared to Configuration-2. It was also observed that for optimal Configuration-1, higher nonlinear stiffness, inerter magnitude and resistance, and lower capacitance and inductance improved the energy harvesting performance. Yang et al. [12] proposed the nonlinear inertance mechanism (NIMs) created by

combining oblique inerters with one common hinged terminal and the other terminals fixed. It was shown that the addition of NIM can enhance the vibration isolation capabilities of a system. The NIM was combined with two different types of isolators, a spring-damper isolator, and a nonlinear quasi-zero-stiffness (QZS) isolator. After the addition of the NIM, the linear isolator showed bending of the frequency response curve toward the low-frequency range and reduction of the original peak values in dynamic response. For QZS systems, after addition of NIM, larger frequency range of small dynamic response amplitude and lower kinetic energy of the mass were observed. In this article, we integrate the inerter and a centrifugal pendulum such that the centrifugal pendulum is parametrically excited by the inerter. The integrated system is referred to as the inerter pendulum vibration absorber (IPVA) for the rest of this article. A variety of systems wherein a pendulum vibration absorber is parametrically excited by a primary structure have been studied extensively. One class of such systems are the autoparametric vibration absorbers, which give rise to interesting nonlinear responses, such as internal resonance [13,14], amplitude-modulated response [15], and chaos [13]. Specifically, they may achieve vibration mitigation by utilizing the transfer of kinetic energy from the primary structure to the pendulum vibration absorber [16–18]. By virtue of the energy transfer phenomenon, autoparametric vibration absorbers have been studied for achieving vibration mitigation and energy harvesting at the same time [19–23]. To achieve the energy transfer phenomenon, however, the natural frequency of the autoparametric vibration absorbers need to be tuned around half the natural frequency of the primary structure, resulting in bulky and heavy designs. Motivated by the studies on the autoparametric vibration absorbers, we incorporate the IPVA in a single degree-of-freedom (SDOF) linear oscillator and study parametric resonance of the IPVA and its application to vibration mitigation.

The rest of this article is organized as follows. In Sec. 2, we will present the design of the IPVA and derive the equations of motion. In Sec. 3, we study the stability of periodic solutions of the system and conduct a bifurcation analysis to determine the boundary of parametric instability. In Sec. 4, direct numerical integration is used to verify the stability boundary obtained from Sec. 3. Section 5 shows the effects of various parameters on the stability boundary. Section 6 compares the proposed system with a linear benchmark and an autoparametric vibration absorber in Ref. [17]. This study is concluded in Sec. 7.

2 Inerter Pendulum Vibration Absorber

In this section, we present the design of the IPVA and derive the corresponding equations of motion. We present two designs: rack-pinion based IPVA and ball screw based IPVA, as shown in Fig. 1. Specifically, the rack-pinion and ball screw IPVA are used to suppress vibrations in the horizontal and vertical directions, respectively. Their working principles are briefly described as follows. Figure 1(a) shows a SDOF linear oscillator (primary structure) that moves in the horizontal direction and is excited by an external force F, which is modeled by a linear spring of stiffness k, a mass M, and a viscous damper of damping coefficient c. The external force is assumed to be harmonic, i.e., $F = F_0 \sin \Omega t$, where F_0 and Ω are the force amplitude and excitation frequency, respectively. Denote by x the displacement of primary structure. To suppress the vibration of primary structure, a rack-pinion based pendulum vibration absorber is considered, which consists of a rack-pinion of radius R, a carrier of radius R_p, and a pendulum vibration absorber of mass m and length r. The rack-pinion is installed between the primary mass and the ground to convert the linear oscillation of the primary mass into rotation of the pinion. As a result, the linear displacement of primary structure and the pinion's angular displacement are related through $x = R\theta$. Note that because the pendulum oscillates in the horizontal plane, the gravity is neglected. Moreover, the carrier is fixed to the pinion, and the pendulum is pivoted on a

point on the circumference of the carrier. Figure 1(c) shows a primary structure that moves in the vertical direction and incorporates the ball screw IPVA. The ball screw is attached between the ground and the primary structure such that linear motion x of the mass is converted to angular motion θ of the ball screw with effective radius $R = L/2\pi$. L refers to the lead value associated with the ball screw as a measure of the ratio of linear displacement of the nut to full rotation of the screw. More specifically, $x = R\theta$, which is the same as the rack-pinion design. A pendulum, of length r and mass m, is also attached perpendicular to the screw, at a radius of R_p from the center of the screw and with an angular displacement of ϕ with respect to the attachment point. Note that two pendulums are shown, but one is to be fixed in place to avoid rotating unbalance. Also, the pendulum moves in the horizontal plane; thus, the gravity is also neglected in the ball screw IPVA.

Both systems consist of two degrees-of-freedom, one associated with the pinion's angular displacement (θ) and the other with the pendulum's angular displacement relative to the pinion (ϕ).

2.1 Equations of Motion.
Although different mechanisms are used, the working principle of both systems are identical. Therefore, their equations of motion are identical. Lagrange's equations are used to derive the equations of motion. First, the total kinetic energy of the system is derived as follows:

$$T = T_M + T_c + T_p \tag{1}$$

where

$$T_M = \frac{1}{2} M (R\dot{\theta})^2, \ T_c = \frac{1}{2} J \dot{\theta}^2,$$

$$T_p = \frac{1}{2} J_p (\dot{\theta} + \dot{\phi})^2 + \frac{1}{2} m \left(R_p^2 \dot{\theta}^2 + r^2 (\dot{\theta} + \dot{\phi})^2 + 2 R_p r \cos(\phi) \dot{\theta} (\dot{\theta} + \dot{\phi}) \right)$$

$$\tag{2}$$

are the kinetic energy of the structure, carrier, and pendulum, respectively. Here, J is the moment of inertia of the carrier-pinion composite and J_p is the moment of inertia of pendulum with respect to its center of mass

$$V = \frac{1}{2} k x^2 = \frac{1}{2} k R^2 \theta^2 \tag{3}$$

To account for energy loss at the pivot point of the pendulum, a torsional viscous damping coefficient c_p is introduced. The virtual work done by the force $F = F_0 \sin(\Omega t)$, the damping torque in the pendulum, and the damping force in the primary mass can be derived as $F\delta x$, $-c_p \dot{\phi} \delta \phi$, and $-c\dot{x}\delta x$, respectively, where c_p and c are the torque damping coefficient in the pendulum and damping coefficient of the viscous damper between primary mass and ground, respectively. Then, the virtual work done by the force F, the damping torque (due to c_p and viscous damping c) are derived as follows:

$$\delta W = FR\delta\theta - c_p \dot{\phi} \delta \phi - c R^2 \dot{\theta} \delta \theta \tag{4}$$

Therefore, the equations of motion of the system obtained using the Lagrange's equations are written as follows:

$$\left(MR^2 + J + mR_p^2 + mr^2 + 2mR_p r \cos\phi \right) \ddot{\theta}$$
$$+ \left(mr^2 + mR_p r \cos\phi + J_p \right) \ddot{\phi} + cR^2 \dot{\theta}$$
$$+ kR^2 \theta - 2mR_p r \dot{\theta} \dot{\phi} \sin\phi - mR_p r \dot{\phi}^2 \sin\phi = F_0 \sin(\Omega t) R,$$
$$\left(mr^2 + J_p \right) \ddot{\phi} + m \left(r^2 + R_p r \cos\phi \right) \ddot{\theta} + c_p \dot{\phi} + mR_p r \dot{\theta}^2 \sin\phi = 0$$

$$\tag{5}$$

It is assumed that the pendulum is made of a point mass such that its moment of inertia with respect to the pivot point is much larger than the pendulum's moment of inertia with respect to its center of mass, i.e., $mr^2 >> J_p$. Furthermore, $J = (m_p + m_c) R_g^2$, where m_p and m_c are
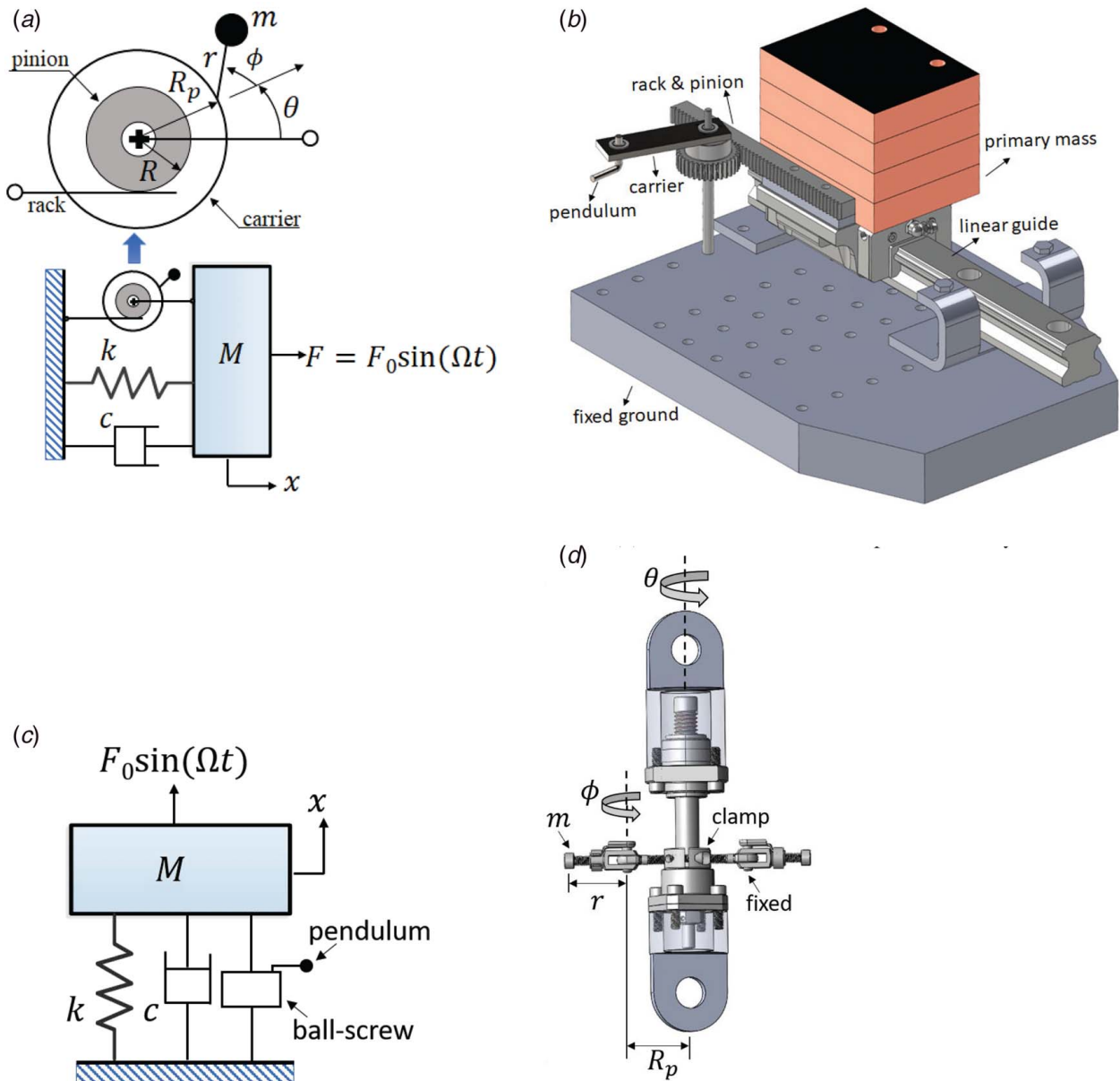
Fig. 1 Rack-pinion and ball screw IPVA systems schematics and CAD realizations: (a) SDOF system incorporating rack-pinion IPVA, (b) CAD realization of rack-pinion IPVA system, (c) SDOF system containing ball screw IPVA system, and (d) CAD realization of the ball screw IPVA system

the pinion mass and carrier mass, respectively, and R_g is the radius of gyration. As the primary mass M is much larger than the sum of m_p and m_c, and as the pinion radius R and the radius of gyration R_g have the same order of magnitude, it is assumed that $MR^2 >> J$. Without loss of generality, J and J_p are neglected. We rescale the time and convert Eq. (5) into a dimensionless form for further analysis using the following parameters:

$$\mu_r = \frac{mR_p^2}{MR^2}, \quad \omega_0 = \sqrt{\frac{k}{M}}, \quad \omega = \frac{\Omega}{\omega_0}, \quad \tau = \omega_0 t, \quad \eta = \frac{r}{R_p}$$

$$\xi = \frac{c}{2\omega_0 M}, \quad \xi_p = \frac{c_p}{2\omega_0 MR^2}, \quad f = \frac{F_0}{MR\omega_0^2}, \quad ()' = \frac{d()}{d\tau}$$

(6)

Denote $\mathbf{x} = [\theta, \phi]^T$ and $\mathbf{f} = [f \sin \omega\tau, 0]^T$. The dimensionless equations of motion are obtained as follows:

$$\mathbf{Mx}'' + \mathbf{Cx}' + \mathbf{Kx} + \mathbf{g}(\mathbf{x}, \mathbf{x}', \mathbf{x}'') = \mathbf{f}$$

(7)

where

$$\mathbf{M} = \begin{bmatrix} 1 + \mu_r(1 + \eta^2) & \mu_r \eta^2 \\ \mu_r \eta^2 & \mu_r \eta^2 \end{bmatrix}, \quad \mathbf{C} = \begin{bmatrix} 2\xi & 0 \\ 0 & 2\xi_p \end{bmatrix}, \quad \mathbf{K} = \begin{bmatrix} 1 & 0 \\ 0 & 0 \end{bmatrix},$$

$$\mathbf{g}(\mathbf{x}, \mathbf{x}', \mathbf{x}'') = \mu_r \eta \begin{bmatrix} (2\theta'' + \phi'') \cos \phi - \phi'(2\theta' + \phi') \sin \phi \\ \theta'' \cos \phi + \theta'^2 \sin \phi \end{bmatrix}$$

(8)

It is worth noting that the strength of the nonlinear inertial terms $\mathbf{g}(\mathbf{x}, \mathbf{x}', \mathbf{x}'')$ is proportional to μ_r and η. The moment of inertia ratio μ_r can be readily magnified by adjusting the ratio R_p/R, thereby creating strong nonlinear inertial effects with a small pendulum mass. For example, for a mass ratio $\frac{m}{M} = 3\%$, a ratio $R_p/R = \sqrt{10}$ leads to $\mu_r = 0.3$, indicating that the inertia effect is magnified by a factor of ten. Furthermore, the pendulum length ratio η is proportional to the length of the pendulum. Therefore, a long pendulum leads to strong nonlinear inertial effects.

3 Parametric Resonance of IPVA

According to the studies on autoparametric resonance, parametric resonance plays an essential role in transferring the kinetic energy of a primary structure to the pendulum vibration absorber [16–18]. As will be demonstrated in Sec. 6, when parametric resonance occurs to the IPVA, a similar energy transfer phenomenon is observed, resulting in vibration mitigation of the primary structure. In this section, we will determine the conditions for which parametric resonance will occur to the IPVA. To this end, we use the harmonic balance method to determine the parametric instability of the system.

3.1 Harmonic Balance Method.
By virtue of the harmonic balance method, periodic solutions of the system are assumed to take the following form:

$$\theta_p(\tau) = \sum_{p=1}^{P} \left(\Theta_p^c \cos\left(\frac{p\omega\tau}{\nu}\right) + \Theta_p^s \sin\left(\frac{p\omega\tau}{\nu}\right) \right)$$

$$\phi_p(\tau) = \Phi_0 + \sum_{p=1}^{P} \left(\Phi_p^c \cos\left(\frac{p\omega\tau}{\nu}\right) + \Phi_p^s \sin\left(\frac{p\omega\tau}{\nu}\right) \right) \tag{9}$$

where Θ_p, Φ_p, and Φ_0 are unknown Fourier coefficients to be determined. Note that $\nu \in \mathbb{N}$ accounts for subharmonics. Furthermore, a constant Φ_0 is included to consider asymmetric oscillation of the centrifugal pendulum [24]. Denote by $\mathbf{x}_p = [\theta_p, \phi_p]^T$ the vector of assumed periodic solutions. After substituting Eq. (9) into the equations of motion (7), we obtain the following residue term:

$$\mathbf{R}(\tau) = \mathbf{M}\mathbf{x}_p'' + \mathbf{C}\mathbf{x}_p' + \mathbf{K}\mathbf{x}_p - \mathbf{g}\left(\mathbf{x}_p, \mathbf{x}_p', \mathbf{x}_p''\right) - \mathbf{f} \tag{10}$$

To obtain an expression relating the Fourier coefficients, a Galerkin procedure [25] is used to project (10) on the orthogonal trigonometric basis, yielding $2P+1$ nonlinear algebraic equations

$$h_0(\hat{\mathbf{x}}) = \int_0^{2\pi\nu/\omega} \mathbf{R}(\tau)\, d\tau = 0, \quad h_p^s(\hat{\mathbf{x}}) = \int_0^{2\pi\nu/\omega} \mathbf{R}(\tau) \sin\left(\frac{p\omega\tau}{\nu}\right) d\tau = 0$$

$$h_p^c(\hat{\mathbf{x}}) = \int_0^{2\pi\nu/\omega} \mathbf{R}(\tau) \cos\left(\frac{p\omega\tau}{\nu}\right) d\tau = 0 \tag{11}$$

where $\hat{\mathbf{x}} = \left[\boldsymbol{\Theta}^T, \boldsymbol{\Phi}^T, \boldsymbol{\Phi_0}\right]^T$, $\boldsymbol{\Theta} = \left[\Theta_1^c, \ldots, \Theta_P^c, \Theta_1^s, \ldots, \Theta_P^s\right]^T$, and $\boldsymbol{\Phi} = \left[\Phi_1^c, \ldots, \Phi_P^c, \Phi_1^s, \ldots, \Phi_P^s\right]^T$. Note that $\mathbf{g}\left(\mathbf{x}_p, \mathbf{x}_p', \mathbf{x}_p''\right)$ will result in composite trigonometric terms such as $\cos\left(\Phi_p^s \sin\left(p\omega\tau/\nu\right)\right)$. These terms can be expanded using the Jacobi–Anger expansion, namely, an infinite series of products of Bessel functions and trigonometric functions [26] (see also Appendix B for the expansion formulas). For the current study, the Jacobi–Anger expansion is truncated at Bessel functions of order up to third to capture the necessary nonlinear effects.

We solve Eq. (11) for the Fourier coefficients using the Newton–Raphson method. Substitution of the Fourier coefficients into Eq. (9) will lead to the periodic solutions. The stability of the periodic solutions will be determined in the next section.

3.2 Stability.
To determine the stability of the periodic solutions, small perturbations are introduced into Eq. (9) as follows:

$$\theta(\tau) = \theta_p(\tau) + \delta_\theta(\tau) \quad \text{and} \quad \phi(\tau) = \phi_p(\tau) + \delta_\phi(\tau) \tag{12}$$

where $|\delta_\theta(\tau)| \ll 1$ and $|\delta_\phi(\tau)| \ll 1$. Denote by $\boldsymbol{\delta} = \left[\delta_\theta, \delta_\phi\right]^T$ the vector of small perturbations. Substitution of Eq. (12) into Eq. (7) and linearization with respect to $\theta_p(\tau)$ and $\phi_p(\tau)$ yield

$$\left(\mathbf{M} + \frac{\partial \mathbf{g}}{\partial \mathbf{x}''}\right)\boldsymbol{\delta}'' + \left(\mathbf{C} + \frac{\partial \mathbf{g}}{\partial \mathbf{x}'}\right)\boldsymbol{\delta}' + \left(\mathbf{K} + \frac{\partial \mathbf{g}}{\partial \mathbf{x}}\right)\boldsymbol{\delta} = \mathbf{0} \tag{13}$$

where the Jacobian matrices $\partial\mathbf{g}/\partial\mathbf{x}''$, $\partial\mathbf{g}/\partial\mathbf{x}'$, and $\partial\mathbf{g}/\partial\mathbf{x}$ are evaluated at $\mathbf{x} = \mathbf{x}_p$, $\mathbf{x}' = \mathbf{x}_p'$, and $\mathbf{x}'' = \mathbf{x}_p''$, respectively, wherever appropriate. Note that the Jacobian matrices are periodic functions of period $T = 2\pi\nu/\omega$, e.g., $\partial\mathbf{g}/\partial\mathbf{x}(\tau) = \partial\mathbf{g}/\partial\mathbf{x}(\tau + T)$. Because Eq. (13) have periodic coefficients, one can use Floquet theory to determine the stability [27]. To this end, Eq. (13) is transformed into the state-space form and numerically integrated using MATLAB's ode45 (based on an explicit Runge–Kutta integration method) over one period T to obtain the fundamental matrix. The absolute and relative tolerance were taken to be 10^{-9} to ensure accuracy. If any eigenvalue of the fundamental matrix has a magnitude greater than unity, the periodic solutions are unstable.

Although Eq. (13) can be used to determine the stability of arbitrary periodic solutions, it is a numerical approach; hence, it is hard to understand how parametric resonance occurs to the IPVA. To gain physical insights, we also use a semi-analytical approach to determine the stability. To that end, we apply a multiple-scale approach to Eq. (13) as follows. Because a compact and lightweight design of the IPVA system is preferred in practical applications, we consider $\mu_r \ll 1$. Assuming that the parameters μ_r, ξ, ξ_p are small quantities, we set $\mu_r = \epsilon\hat{\mu}_r$, $\xi = \epsilon\hat{\xi}$, $\xi_p = \epsilon\hat{\xi}_p$ and introduce the following asymptotic expansions:

$$\delta_{\theta,\phi}(\tau) = \delta_{\theta,\phi}^{(0)}(\tau_0, \tau_1, \ldots) + \epsilon\delta_{\theta,\phi}^{(1)}(\tau_0, \tau_1, \ldots) + \cdots$$

$$\tau_k = \epsilon^k\tau, \quad k = 0, 1, \ldots$$

$$\frac{d}{d\tau} = \frac{\partial}{\partial\tau_0} + \epsilon\frac{\partial}{\partial\tau_1} + \cdots \tag{14}$$

where $|\epsilon| \ll 1$ is a small bookkeeping parameter.

After substituting Eq. (14) into Eq. (13) and collecting terms that will lead to parametric instabilities, the equation obtained in order $O(\epsilon^0)$ is expressed as follows:

$$\frac{\partial^2 \delta_\theta^{(0)}}{\partial\tau_0^2} + \delta_\theta^{(0)} = 0, \quad \frac{\partial^2 \delta_\phi^{(0)}}{\partial\tau_0^2} + \frac{2\hat{\xi}_p}{\hat{\mu}_r\eta^2}\frac{\partial\delta_\phi^{(0)}}{\partial\tau_0} + \frac{A(\mathbf{x}_p)}{\eta}\delta_\phi^{(0)} = 0 \tag{15}$$

where

$$A(\mathbf{x}_p) = \cos(\phi_p)\left(\theta_p'\right)^2 - \sin(\phi_p)\theta_p'' \tag{16}$$

is a periodic coefficient of period T. It is worth noting that the first equation in Eq. (15) shows that $\delta_\theta^{(0)}$ are stable harmonic functions. Therefore, the stability of the periodic solutions are determined by the second equation in Eq. (15).

When the nonlinearity is weak, periodic solutions (9) are dominated by primary harmonics, i.e., $P = 1$ and $\nu = 1$. As Eq. (15) is derived by the multiple-scale approach, it is accurate when the nonlinearity is weak. Therefore, in addition to Eq. (13) (Floquet theory), Eq. (15) is used to determine the boundary of parametric instability for periodic solutions of primary harmonics, which will explain how parametric resonance occurs to the IPVA. Thus, $P = 1$ and $\nu = 1$ are substituted in Eq. (9) to obtain $\theta_p = \Theta_1^c \cos(\omega\tau) + \Theta_1^s \sin(\omega\tau)$ and $\phi_p = \Phi_0 + \Phi_1^c \cos(\omega\tau) + \Phi_1^s \sin(\omega\tau)$. After substituting these expressions of Θ and Φ into Eq. (15) and expanding in terms of Bessel functions up to third order, we arrive at a damped Mathieu equation as follows:

$$\frac{\partial^2 \delta_\phi^{(0)}}{\partial\tau_0^2} + \frac{2\xi_p}{\mu_r\eta^2}\frac{\partial\delta_\phi^{(0)}}{\partial\tau_0} + \frac{u(\hat{\mathbf{x}})}{\eta}\delta_\phi^{(0)} + \frac{v(\hat{\mathbf{x}})}{\eta}\cos(\omega\tau - \gamma)\delta_\phi^{(0)} = 0 \tag{17}$$

where

$$u(\hat{\mathbf{x}}) = \frac{\omega^2\Theta_1 c(\Phi_0)}{2}\{\Theta_1[J_0(\Phi_1) + J_2(\Phi_1)s(2\alpha)] + 2J_1(\Phi_1)s(\alpha)\},$$

$$v(\hat{\mathbf{x}})^2 = [b_0b_1 + 2b_2(b_1 + b_3)]c(\alpha) + (2b_0b_2 + 2b_1b_3 - b_1^2)c(2\alpha)$$

$$+ (2b_0b_3 - b_1b_2)c(3\alpha) - b_1b_3c(4\alpha) + b_0^2 + \frac{5b_1^2}{4} + b_2^2 + b_3^2,$$

$$b_0 = s(\Phi_0)\Theta_1\omega^2 J_0(\Phi_1), \quad b_1 = -s(\Phi_0)\Theta_1^2\omega^2 J_1(\Phi_1),$$

$$b_2 = -s(\Phi_0)\Theta_1\omega^2 J_2(\Phi_1), \quad b_3 = -s(\Phi_0)\Theta_1^2\omega^2 J_3(\Phi_1)$$

$$\Theta_1 = \sqrt{(\Theta_1^c)^2 + (\Theta_1^s)^2}, \quad \Phi_1 = \sqrt{(\Phi_1^c)^2 + (\Phi_1^s)^2}, \tag{18}$$

$$\alpha = \tan^{-1}\left(\frac{\Phi_1^s\Theta_1^c - \Phi_1^c\Theta_1^s}{\Phi_1^c\Theta_1^c + \Phi_1^s\Theta_1^s}\right) \tag{19}$$

where $c(\cdot) = \cos(\cdot)$, $s(\cdot) = \sin(\cdot)$, and $J_n(\cdot)$ denotes Bessel functions of the first kind of order n. Note that the detail of phase angle γ is not provided because γ is irrelevant to stability. There are two things worth noting in Eqs. (17) and (19). First, $b_0 = b_1 = b_2 = b_3 = 0$ or $v(\hat{\mathbf{x}}) = 0$ when $\Phi_0 = 0$. Because $v(\hat{\mathbf{x}})$ is the magnitude of parametric excitation, no parametric instabilities can occur when $v(\hat{\mathbf{x}}) = 0$. In other words, nonzero asymmetric oscillation, i.e., $\Phi_0 \neq 0$, is a necessary condition for parametric instabilities. Second, the linear stiffness term $u(\hat{\mathbf{x}})$ is composed of nonlinear inertial coupling induced by the carrier motion Θ_1. As the nonlinear inertial coupling results in linear stiffness per se, the pendulum can have parametric resonance without having any linear stiffness. Compared to the autoparametric vibration absorbers, which would need to have low linear stiffness to tune their natural frequency around half the natural frequency of the primary structure [16–18], the nonlinear inertial coupling of the IPVA enables compact designs.

To determine the boundary of parametric instability, Eq. (17) is transformed to the standard form of Mathieu equation [13]:

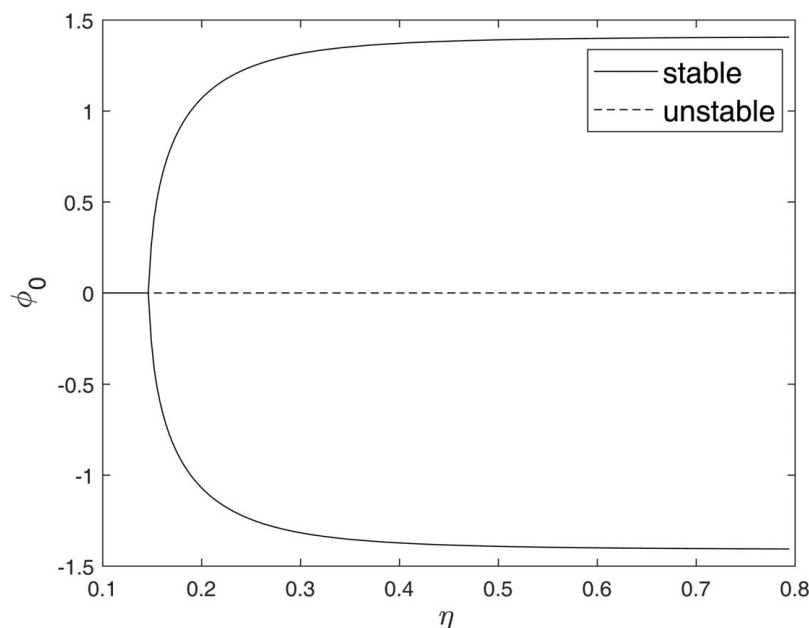$$\frac{\partial^2\Psi}{\partial w^2} + p(\hat{\mathbf{x}})\Psi - 2q(\hat{\mathbf{x}})\cos(2w)\Psi = 0 \tag{20}$$

where

$$\Psi = \delta_\phi^{(0)}\exp\left(\frac{2\hat{\xi}_p w}{\hat{\mu}_r\eta^2\omega}\right), \quad 2w = \omega\tau - \gamma$$

$$p(\hat{\mathbf{x}}) = \frac{4u(\hat{\mathbf{x}})}{\eta\omega^2} - \frac{4\hat{\xi}_p^2}{\hat{\mu}_r^2\eta^4\omega^2}, \quad q(\hat{\mathbf{x}}) = -\frac{2v(\hat{\mathbf{x}})}{\eta\omega^2} \tag{21}$$

The boundary of parametric instability for Eq. (20) corresponds to the transition curves in the $p - q$ plane [28]. Because we seek the boundary that occurs with low force magnitudes, we compute the transition curve that occurs with the lowest p and q values. Mathematically, this transition curve is expressed as $p = \mathcal{A}_1(q)$, where $\mathcal{A}_1(q)$ are the characteristic values for even Mathieu functions with characteristic exponent 1 and parameter q [28]. In this article, $\mathcal{A}_1(q)$ is computed by the "MathieuCharacteristicA" function of WOLFRAM MATHEMATICA 11.3. Note that p and q are functions of f and ω. Therefore, $p = \mathcal{A}_1(q)$ is solved with Eq. (11) simultaneously to yield the transition curves in the $f - \omega$ plane.

3.3 Pitchfork Bifurcation. As mentioned in Sec. 3.2, nonzero asymmetric oscillation, i.e., $\Phi_0 \neq 0$, is necessary to induce parametric instabilities. To determine when it occurs, $\theta_p = \Theta_1^c\cos(\omega\tau) + \Theta_1^s\sin(\omega\tau)$ and $\phi_p = \Phi_0 + \Phi_1^c\cos(\omega\tau) + \Phi_1^s\sin(\omega\tau)$ are substituted into Eq. (13) to solve for stable periodic solutions with $\Phi_0 \neq 0$. We use the pendulum length ratio η as the bifurcation parameter to obtain a bifurcation diagram that shows the parameter space, wherein $\Phi_0 \neq 0$ will occur. To track the bifurcation points with varying η, a bifurcation tracking algorithm that is based on arclength continuation is used with Eq. (13); see Appendix A for the detail. Figure 2 shows a bifurcation diagram of Φ_0 with varying η. Three branches of the bifurcation were obtained using three different sets of initial conditions (one corresponding to each branch, namely, the lower, middle, and upper). It can be observed that Φ_0 undergoes a supercritical pitchfork bifurcation at a critical value of η. After this critical value of η, $\Phi_0 \neq 0$ and parametric instabilities become possible. For the rest of this article, we will only explore parametric instabilities with the parameters that lead to $\Phi_0 \neq 0$.


Fig. 2 Pitchfork bifurcation of ϕ_0 for $f = 0.007$, $\mu_r = 0.2$, $\omega = 0.9$, $\xi = \xi_p = 0.005$
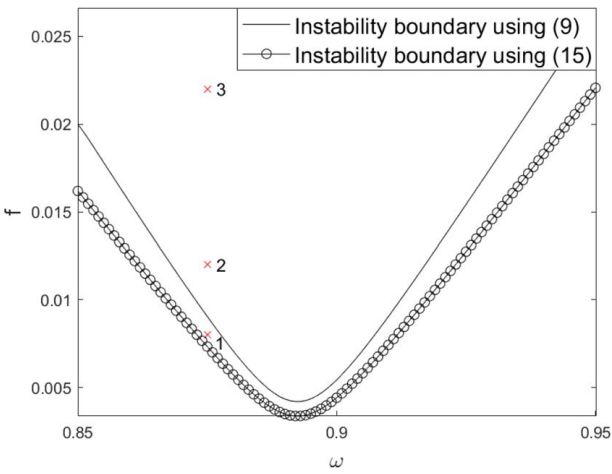
Fig. 3 Parametric instability boundary for $\eta = 0.3$, $\mu_r = 0.25$, $\xi = 0.005$, $\xi_p = 0.005$

3.4 Period Doubling Bifurcation. Within the parameter space wherein $\Phi_0 \neq 0$ exist, the boundary of parametric instability is computed in the $f - \omega$ plane. To find an initial bifurcation point for the bifurcation tracking algorithm described in Appendix A, $\omega = 0.8$ is set and Eq. (13) is repeatedly used to compute the Floquet multipliers as f decreases until the maximum magnitude of the Floquet multipliers becomes unity. Afterward, the bifurcation tracking algorithm will generate the boundary as described in Appendix A. To verify whether the boundary is indeed of parametric instability, the Mathieu equation (20) is used to generate the transition curve as described in Sec. 3.2. The boundary and transition curve for a set of parameters are shown in Fig. 3. As shown, although the transition curve underestimates the boundary, they are in qualitative agreement. Specifically, the discrepancy between the two curves increases as the force magnitude f increases. Because the transition curve is predicted by the perturbation method, it is reasonable that it is more accurate for small force magnitudes. Thus, the comparison verifies the claim that the boundary indicates parametric instability. To gain more insight, the Floquet exponents corresponding to a few points on the boundary are computed and found equal to $\pm i\pi/T$, where $i = \sqrt{-1}$. According to Ref. [29], this indicates period doubling bifurcation. Since periodic doubling bifurcation is a co-dimension one bifurcation, it is a curve in a parameter plane [30]. Therefore, the parametric instability boundary is in fact a boundary of period doubling bifurcation. When this bifurcation occurs, the pendulum oscillation will have subharmonics of $\omega/2$, i.e., $\nu = 2$ in Eq. (9). It is worth noting that the autoparametric vibration absorbers also have a similar bifurcation behavior, that is, subharmonics of half excitation frequency induced by parametric instabilities [16–18].

Within the parameter space wherein subharmonics of $\omega/2$ exist, the stability of the subharmonics can be further investigated. Preliminary investigations indicates the presence of another period doubling bifurcation, implying that subharmonics of quarter
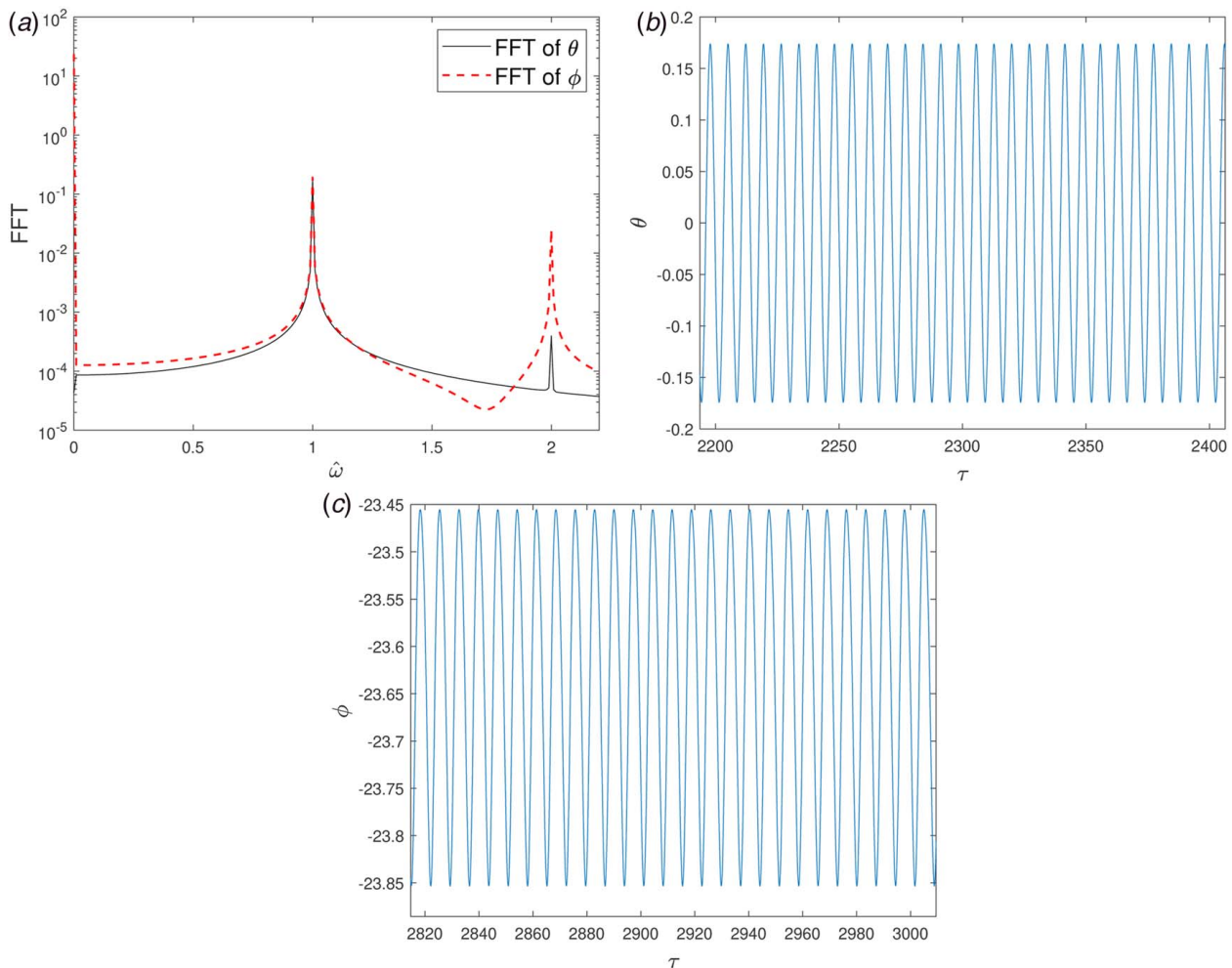
Fig. 4 FFT and time series of periodic solutions at point 1 in Fig. 3: (a) FFT at point 1, (b) time series of θ at point 1, and (c) time series of ϕ at point 1
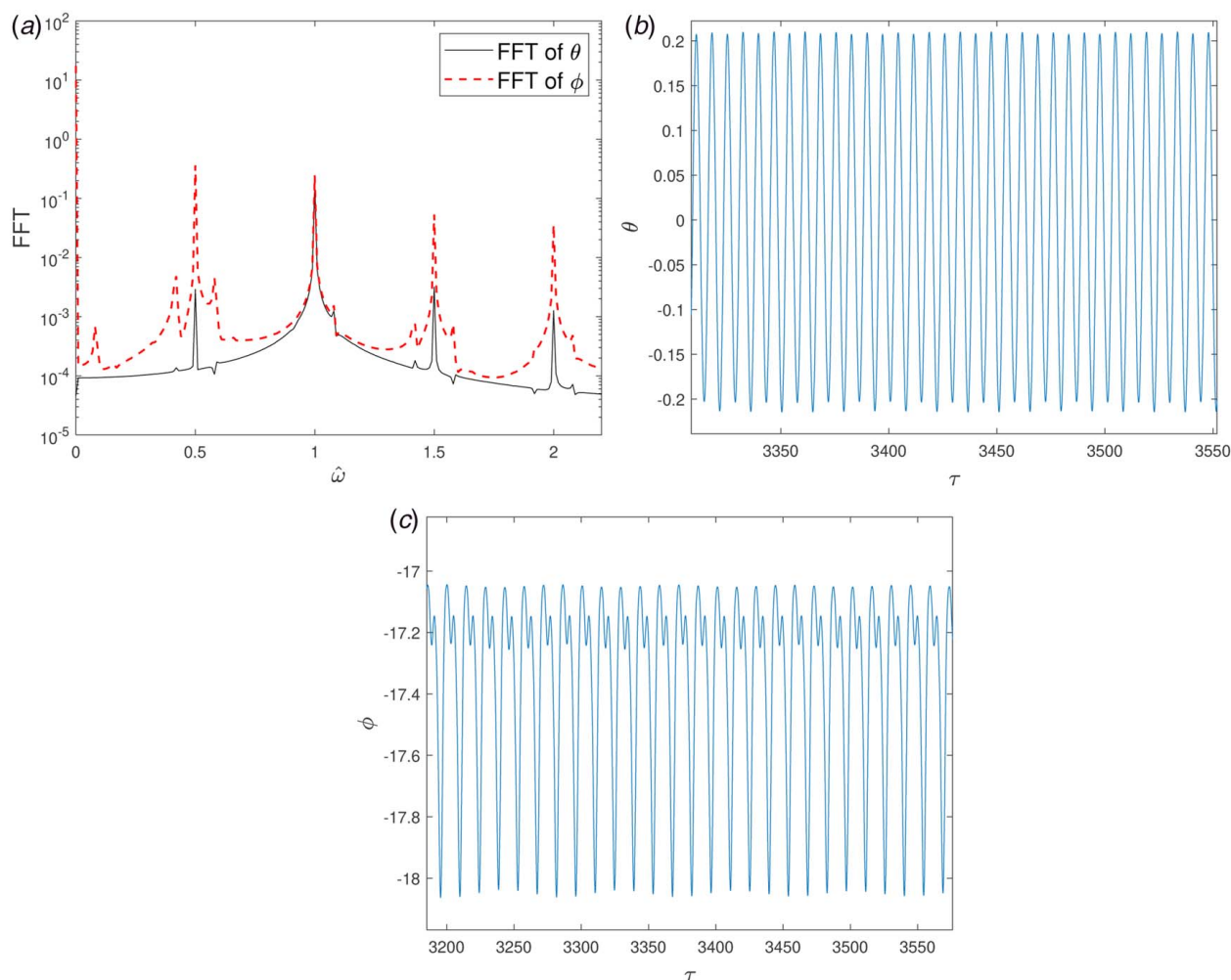
Fig. 5   FFT and time series of periodic solutions at point 2 in Fig. 3: (*a*) FFT at point 2, (*b*) time series of *θ* at point 2, and (*c*) time series of *φ* at point 2

frequency will appear. Therefore, it is hypothesized that there exists a cascade of period doubling bifurcations in the $f - \omega$ space, which eventually leads to chaotic motions of the system. Determination of the boundary of this additional period doubling bifurcation, however, is out of the scope of this paper.

Figure 3 is a bifurcation diagram that shows the parameter space for qualitatively different solutions, defined by the instability boundary. By locating the parameters in Fig. 3, the qualitative behavior of the corresponding solutions can be predicted. For example, ×2 resides in the parameter space just above the boundary. Accordingly, periodic solutions of primary harmonics along with subharmonics of excitation frequency are predicted at ×2. Next, we verify the predictions by Fig. 3 by direct numerical integration.

4   Numerical Demonstration

To verify the bifurcation analysis in Sec. 3.4, numerical integration (MATLAB's ODE45) is used to obtain the solutions of Eq. (7) at three representative points in Fig. 3 (denoted by markers "×" followed by numbers, e.g., ×2). Among these three points, points ×1 and ×2 lead to periodic solutions, whereas point ×3 leads to nonperiodic solutions. The fast Fourier transform (FFT) of the periodic solutions are computed to reveal the frequency components, which are shown in Figs. 4(*a*), 5(*a*), and 6(*a*). On the other hand, a time series of the solutions are presented to show the dynamical behaviors, shown in Figs. 4(*a*), 5(*b*), 6(*b*), 4(*c*), 5(*c*), and 6(*c*). Note that the frequencies $\hat{\omega}$ of the FFT are normalized with respect to the

excitation frequency. It follows that primary harmonics correspond to components at $\hat{\omega} = 1$, subharmonics of half excitation frequency correspond to components at $\hat{\omega} = 0.5$, etc.

There are several things worth noting in Figs. 3–6. First, the prediction at point ×1 is in good agreement with the numerical solutions. As shown in Fig. 3, point ×1 is below the instability boundary. It is expected that the periodic solutions are dominated by primary harmonics. This prediction is verified by Fig. 4, which shows that the periodic solutions at point ×1 have the largest components at $\hat{\omega} = 1$, corresponding to primary harmonics. Furthermore, in Fig. 3, as we increase the value of f and reach point ×2, the primary harmonics undergo a period doubling bifurcation. As a result, subharmonics of half excitation frequency should arise. As shown in Fig. 5, subharmonics of half excitation frequency indeed exist, which verifies the prediction in Fig. 3. Second, the parameters at ×3 lead to strong nonperiodic solutions composed of both oscillation and intermittent rotations of the pendulum, as shown in Figs. 6(*c*) and 7(*c*). Similar nonperiodic solutions are also observed in autoparametric resonance vibration absorbers [18].

In addition to FFT, the Poincaré sections are used to demonstrate the period doubling bifurcations predicted by Fig. 3. The Poincaré sections are computed by the Hénon trick [31], which are defined as follows:

$$P^n(\mathbf{x}_0) = \mathbf{x}_n\big(\tau_0 + 2n\pi/\omega; \mathbf{x}_{n-1}, \tau_0\big), \quad n = 1, 2, \ldots \quad (22)$$

where $\mathbf{x}_{n-1}$ and $\mathbf{x}_n$ are the solutions of the system (7), which pass through the Poincaré section at time $\tau = \tau_0 + 2(n-1)\pi/\omega$ and
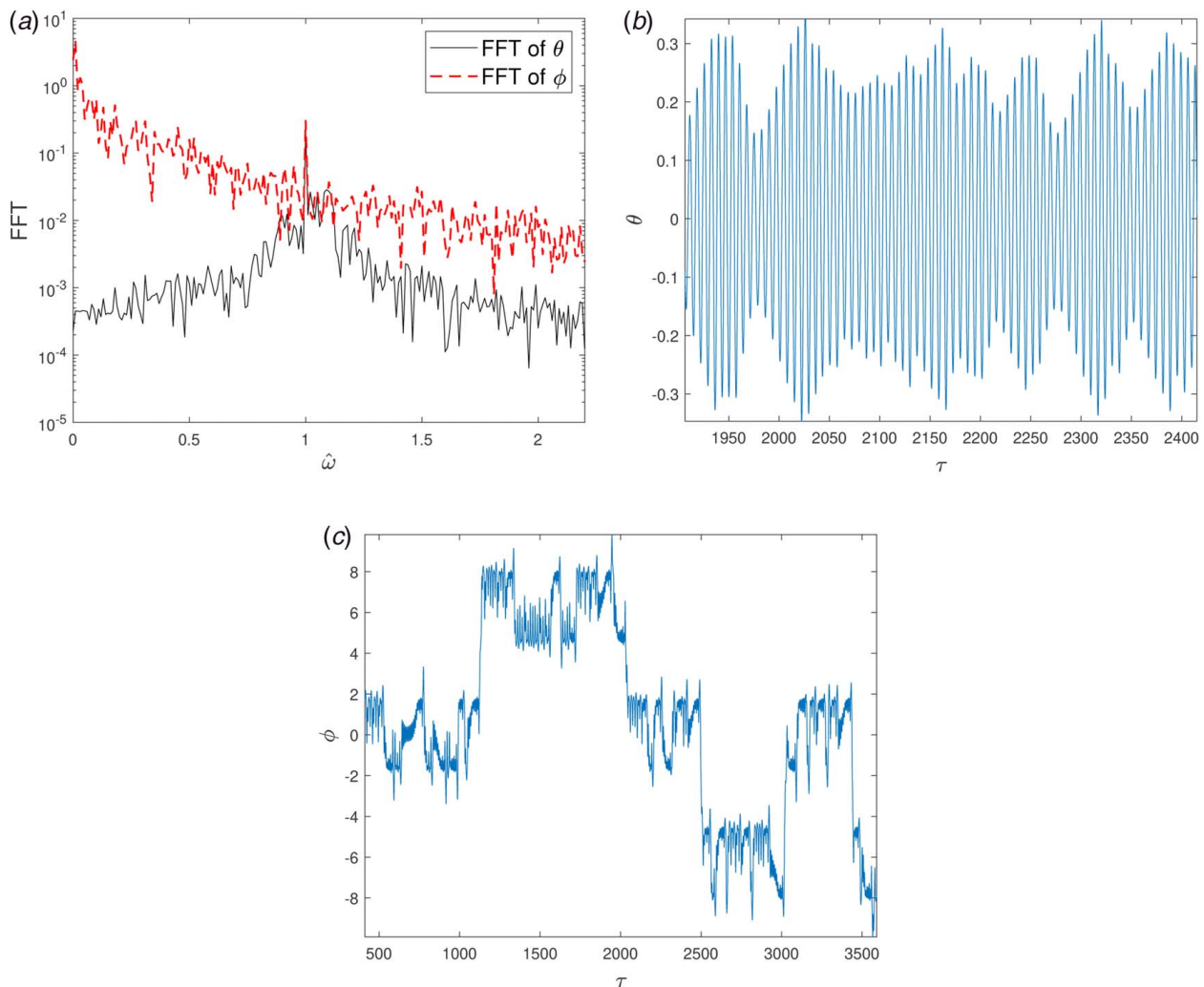
Fig. 6 FFT and time series of nonperiodic solutions at point 3 in Fig. 3: (a) FFT at point 3, (b) time series of θ at point 3, and (c) time series of ϕ at point 3

$\tau = \tau_0 + 2n\pi/\omega$, respectively. Successively, the points $\mathbf{x}_0$, $\mathbf{x}_1 = P(\mathbf{x}_0)$, $\mathbf{x}_2 = P^2(\mathbf{x}_0)$, ... correspond to the intersection of the trajectory $\mathbf{x}(\tau; \mathbf{x}_0, \tau_0)$ with the sections at $\tau = \tau_0$, $\tau_0 + 2\pi/\omega$, $\tau_0 + 4\pi/\omega$, ..., respectively.

To demonstrate the period doubling bifurcation, Poincaré sections corresponding to point ×1 and ×2 are plotted in Fig. 7. As shown in Fig. 7(a), ×1 leads to a fixed point on the Poincaré section, corresponding to period-1 solutions. Figure 7(b), on the other hand, shows two fixed points, corresponding to period-2 solutions. Therefore, it is clear that the system has undergone a period doubling bifurcation when moving from ×1 to ×2.

5 Parametric Studies

In this section, we analyze the effect of the parameters on the instability boundary. We consider four parameters in Eq. (6), namely, μ_r, η, ξ, and ξ_p. It can be seen that these parameters can be varied independently of each other. Therefore, we will observe the effect by varying one parameter while keeping the other parameters constant. We start by increasing the value of η while keeping the others constant. From Fig. 8, it can be observed that increasing η does not make any significant change in the lowest f value for parametric instability to occur, which corresponds to the vertex of the boundaries. That means that value of η should not influence the energy transfer capabilities of the system by a lot. However, a minimum threshold value of η is required for period-doubling

bifurcation to occur as discussed in Sec. 3.3. We next vary μ_r. From Fig. 9, it can be observed that the required values of f to attain parametric instability decrease as μ_r increases. This can be attributed to the fact that the inertia supplied by the pendulum vibration absorber increases as the mass amplification factor μ_r is increased. The value of μ_r can be controlled by changing the ratio R_p/R, which can be adjusted by changing the carrier radius (R_p).

While keeping the other parameters constant, we vary the viscous damping ratio ξ and observe its effects. From Fig. 10, it can be seen that the requirement of f to achieve nonlinear energy transfer increases with the increase in the viscous damping. In a similar fashion, we vary the ξ_p while keeping the other parameters constant. We see that the values of f required to achieve parametric instability increase as the viscous damping increases. The observations on the effects of both viscous damping match well with the effect of viscous damping on parametric instability—the larger the viscous damping, the larger the force it takes to cause parametric instability [28].

Last but not least, the parameter μ_r has a significant influence on the instability boundary, as demonstrated in Sec. 5. As shown in Fig. 9, a larger μ_r not only leads to lower force magnitudes required to cause parametric resonance but a wider frequency bandwidth of parametric resonance, which is beneficial in terms of vibration mitigation. The parameter μ_r can be readily increased by changing the ratio of R_p/R without incurring the large weight to the system, which is attributed to the mass amplification effect of the inerter.
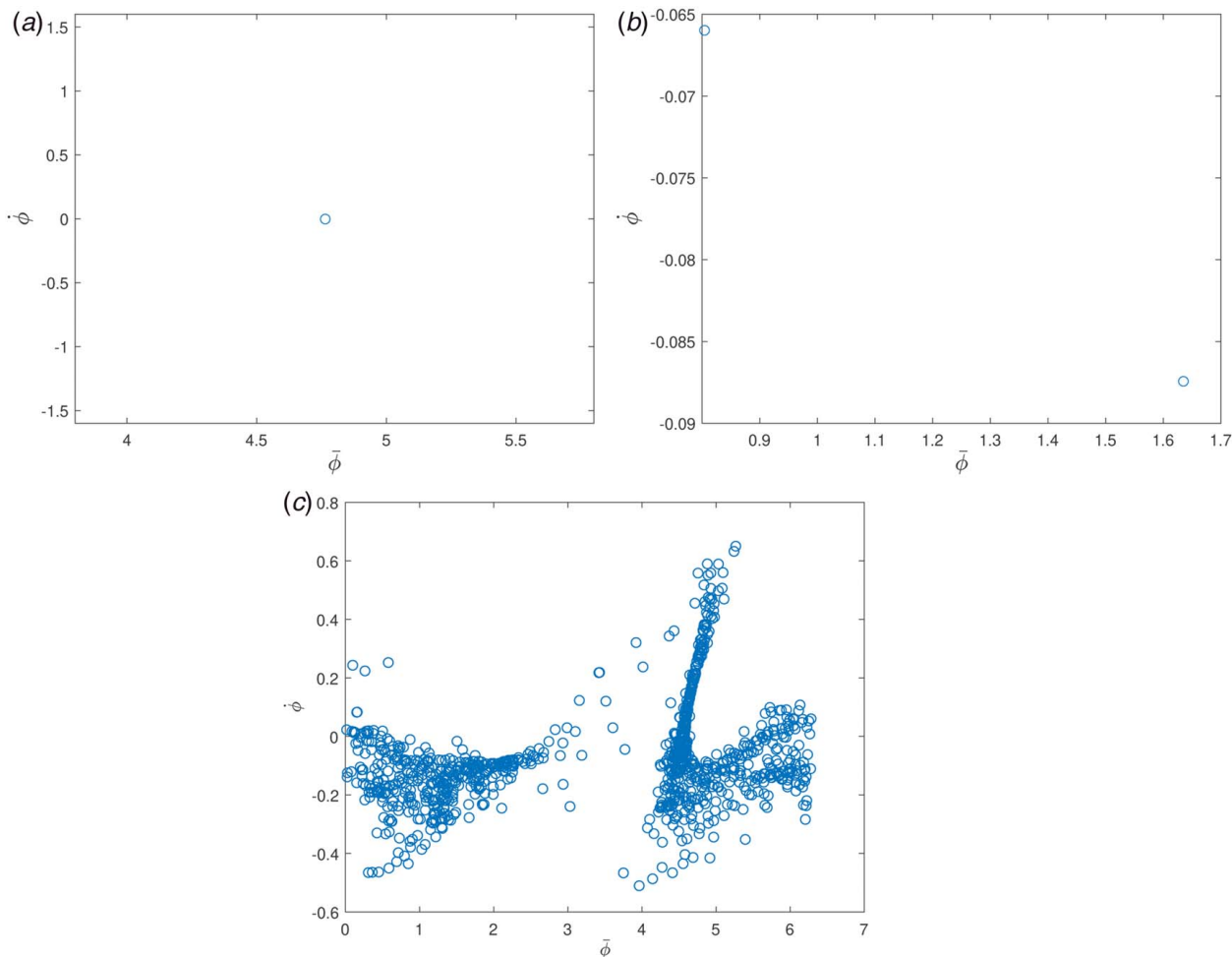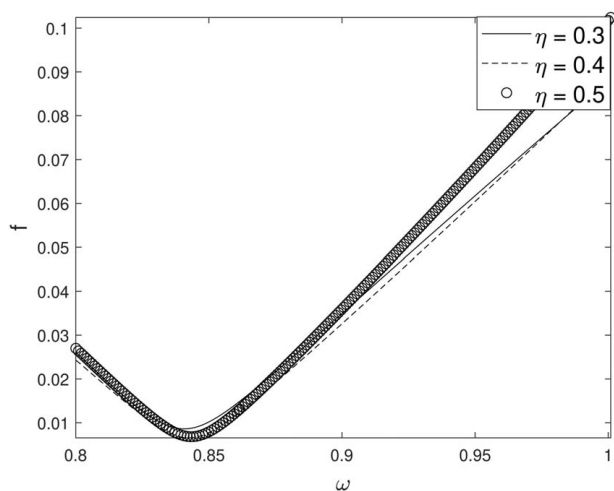
Fig. 7 Poincare section at points 1–3 as marked in Fig. 3. The value of ϕ is normalized between 0 and 2π: (a) Poincaré section at point 1, (b) Poincaré section at point 2, and (c) Poincaré section at point 3

6 Discussion

In the beginning of this study, it was proposed that a nonlinear energy transfer phenomenon similar to autoparametric resonance takes place when the parametric instability occurs. To demonstrate this, we compare the proposed system with two systems, a linear

Fig. 8 Parametric instability boundary for $\mu_r = 0.4$, $\xi = 0.005$, $\xi_P = 0.01$ for various values of η

benchmark and an autoparametric vibration absorber with parametrically excited pendulum [17]. The linear system here is characterized by locking the pendulum at its initial position ($\phi = 0$), effectively removing all the nonlinearities in the system. By setting $\phi = \phi' = \phi'' = 0$ in Eq. (7), the equation of motion of the linear system is written as follows:

$$\left[1 + \mu_r\left(1 + \eta^2 + 2\eta\right)\right]\theta'' + 2\xi\theta' + 2\xi_p\theta' + \theta = f\sin\omega\tau \qquad (23)$$

By using $\theta = \frac{1}{2}\Theta e^{i\omega\tau} + c.c.$, the equation can be solved to obtain

$$\Theta = \left|\frac{f}{2i\omega\left(\xi + \xi_p\right) + 1 - \omega^2\left[1 + \mu_r\left(1 + \eta^2 + 2\eta\right)\right]}\right| \qquad (24)$$

We computed the root-mean-square (rms) of the IPVA system and compared it with the linear system. The comparison is shown in Fig. 12. The response from the 2401th to 3000th cycle was used to compute the rms to eliminate transient effects. The IPVA parameters used in Figs. 12(*a*) and 12(*b*) correspond to Figs. 3 and 11, respectively.

Several things are worth noting in Fig. 12. First, it is shown that the response of the primary structure flattens for a range of excitation frequencies. In comparison with the response of the linear system, the IPVA shows significant vibration suppression with the flattening region. For example, as shown in Fig. 12(*b*), θ for
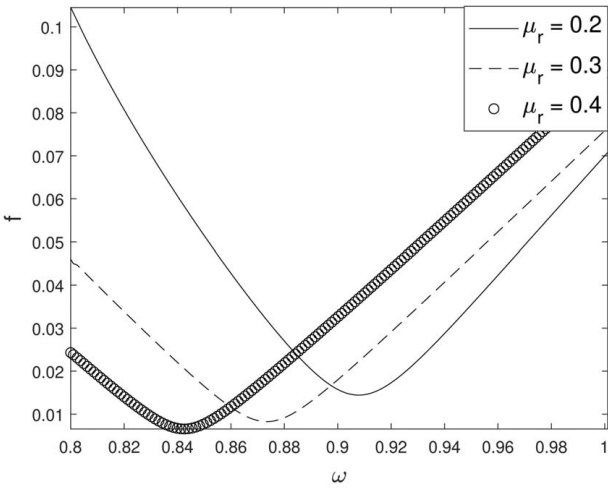
Fig. 9 Parametric instability boundary for $\eta = 0.4$, $\xi = 0.005$, $\xi_p = 0.01$ for various values of μ_r
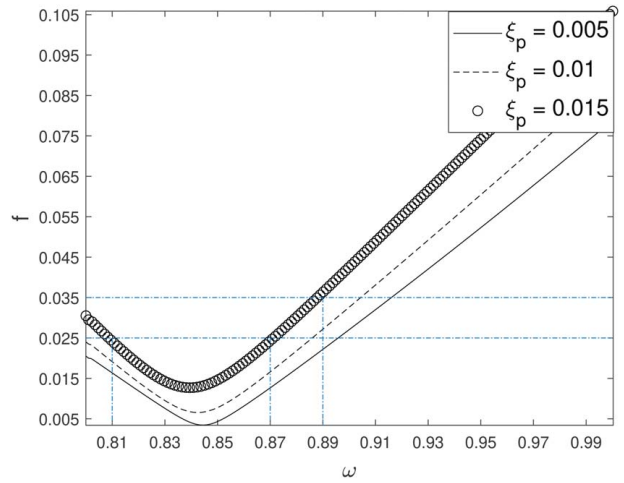

Fig. 11 Parametric instability boundary for $\eta = 0.4$, $\mu_r = 0.4$, $\xi = 0.005$ for various values of ξ_p
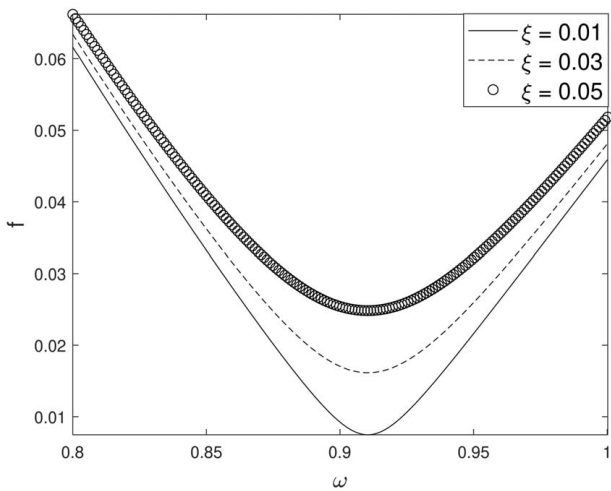

Fig. 10 Parametric instability boundary for $\eta = 0.3$, $\mu_r = 0.2$, $\xi_p = 0.005$ for various values of ξ

$f_0 = 0.025$ flattens for $\omega \in [0.81, 0.87]$. In comparison with Figs. 3 and 11, it is clear that the flattening occurs when the system is within the parametric instability boundary. For example, as shown in Fig. 11, when $\xi_p = 0.015$ and $f_0 = 0.025$, the system is within the parametric instability boundary for $\omega \in [0.81, 0.87]$. This observation agrees with Fig. 12(*b*). Second, within the flattening region, the response of the primary structure barely increases despite an increase in the force magnitude, suggesting a saturation phenomenon similar to autoparametric vibration absorbers [23] and nonlinear vibration absorbers with quadratic nonlinearities [32]. Note that the response of the IPVA system in Fig. 12(*b*) is nonperiodic for $f = 0.035$ within a range of ω; thus, different initial conditions may lead to different rms responses. To examine the effect of initial conditions, ten rms responses were computed and plotted at *six* discrete ω values, each corresponding to a different initial condition vector $[\theta, \phi, \dot{\theta}, \dot{\phi}]^T$ that was randomly chosen from a standard normal distribution with zero mean and a unit standard deviation; see the inset in Fig. 12(*b*).

Next, we compare IPVA with the autoparametric vibration absorber shown in Fig. 13. Because the autoparametric system oscillates in the vertical direction, the ball screw IPVA is considered
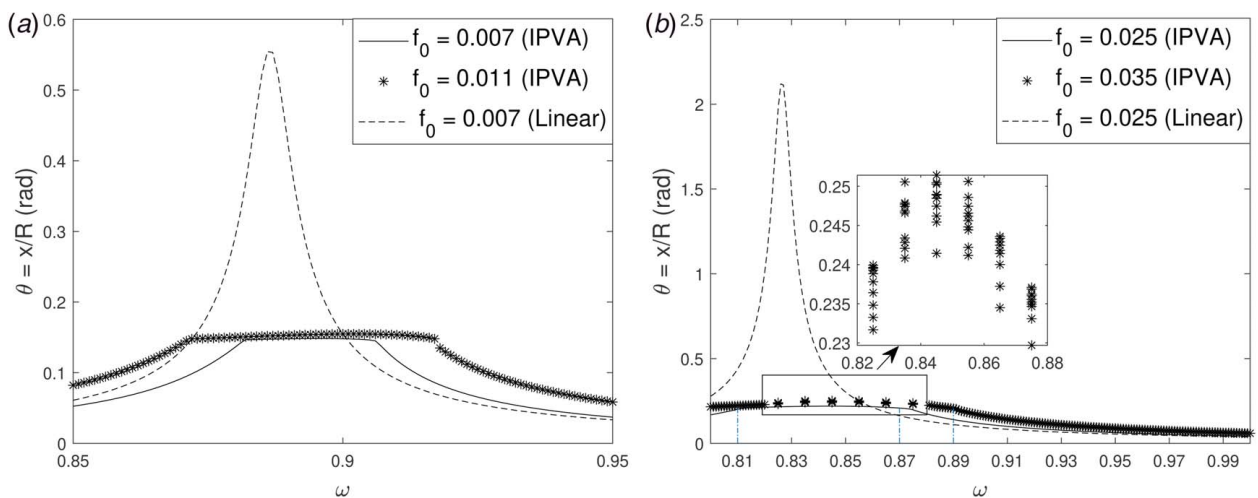

Fig. 12 Comparison of IPVA with the linear system for various parameters: (a) comparison of linear system ($f_0 = 0.007$) with IPVA for different f_0 values for $\eta = 0.3$, $\mu_r = 0.25$, $\xi = 0.005$, and $\xi_p = 0.005$ and (b) comparison of linear system ($f_0 = 0.025$) with IPVA for different f_0 values for $\eta = 0.4$, $\mu_r = 0.4$, $\xi = 0.005$, and $\xi_p = 0.015$
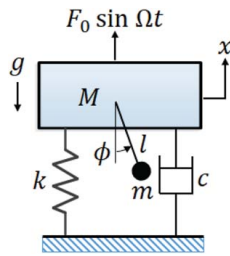
Fig. 13   The autoparametric vibration absorber [17]

hereinafter. The equation of motion of the autoparametric system is written as follows [17]:

$$(M + m)\ \ddot{x} + c\dot{x} + kx + ml\left(\ddot{\phi}\sin\phi + \dot{\phi}^2\cos\phi\right) = F_0\sin(\Omega t)$$
$$ml^2\ddot{\phi} + c_a\dot{\phi} + \left(mgl + ml\ddot{x}\right)\sin\phi = 0$$
(25)

where x and ϕ represent the primary structure displacement and pendulum angular displacement, respectively, M, k, and c are the mass, stiffness, and viscous damping coefficient of the primary structure, respectively, and m and l are the pendulum mass and length, respectively. Furthermore, a viscous damping coefficient c_a is introduced to account for energy loss at the pivot point of the pendulum.

According to Ref. [17], when the natural frequency of the pendulum is tuned around half of the natural frequency of the primary structure, the system shows autoparametric resonance for a certain set of parameters when excited harmonically. This autoparametric resonance results in energy transfer from the primary structure to the pendulum, thereby achieving vibration suppression of the primary structure. Because the IPVA system and the autoparametric system achieve vibration suppression in a similar way, the latter is an ideal benchmark system for comparison. For a fair comparison, the primary structure parameters, excitation force magnitude, and pendulum mass are kept identical in both systems. Specifically, primary mass $M = 5$ kg, natural frequency of the primary structure $\omega_0 = \sqrt{k/M} = 4\pi$ rad/s, pendulum mass $m = 0.5$ kg, force magnitude $F_0 = 0.491$ N, and $\xi = 0.005$ or $\xi = 0.01$. Note that two values of ξ are considered to examine the performance of the IPVA when the damping ratio of the primary structure changes. The remaining parameters pertaining to the autoparametric system are $c_a = 8.68 \times 10^{-5}$ N·m·s and $l = 12.42$ cm, which were taken

from Ref. [17]. Specifically, the pendulum length was chosen to achieve autoparametric resonance, and the pendulum damping coefficient was determined from $\xi_a = c_a/(2ml^2\omega_p) = 0.05$, where $\omega_p = \sqrt{g/l}$ is the natural frequency of the pendulum. The remaining parameters pertaining to the IPVA system are R, R_p, and r. Three sets of R, R_p, and r were chosen as follows: (a) $R = 2.49$ cm, $R_p = 4.97$ cm, and $r = 1.99$ cm; (b) $R = 1.78$ cm, $R_p = 3.55$ cm, and $r = 1.42$ cm; and (c) $R = 2.07$ cm, $R_p = 4.14$ cm, and $r = 1.66$ cm. These three sets are labeled as IPVA (a), IPVA (b), and IPVA (c), respectively, in Figs. 14 and 15. These three sets all lead to $\mu_r = 0.4$ and $\eta = 0.4$ and lead to $f = 0.025$, $f = 0.035$, and $f = 0.030$, respectively. In this way, the dependence of the IPVA on different values of f will be examined. The rms response of the IPVA system and autoparametric system were computed using the same direct numerical integration scheme with the same settings that were used to generate Fig. 12. The effects of initial conditions were examined for both systems when their responses were observed to be nonperiodic using the same method used to obtain Fig. 12(b).

There are several things worth noting in Fig. 14. First, it can be clearly seen that the response curve of the primary structure displacement x for both IPVA (a) and IPVA (b) flattens for a range of ω, which demonstrates the energy transfer phenomenon for two different sets of parameters. Specifically, IPVA (b) has a more compact design (smaller R, R_p, and r) and shows better performance. Although the autoparametric system shows similar vibration suppression, both IPVA (a) and IPVA (b) outperform it. Second, let us examine the pendulum response in Fig. 14(b). As seen, for both IPVA (a) and IPVA (b), the pendulum response significantly increases within the ω range of parametric instability ($\omega \in [0.81, 0.87]$ for IPVA (a) and $\omega \in [0.80, 0.89]$ for IPVA (b)), indicating that the kinetic energy of the primary structure transfers to the pendulum, resulting in the response flattening observed in Fig. 14(a). It is noteworthy that both IPVA (a) and IPVA (b) have a larger pendulum angular velocity than the autoparametric system. Similarly, Figs. 15(a) and 15(b) show the comparison of IPVA (c) with the autoparametric system for $\xi = 0.01$. As can be observed, IPVA (c) outperforms the autoparametric system in terms of vibration suppression. Furthermore, it also leads to a larger pendulum angular velocity.

In addition to better vibration suppression, the IPVA system has two other advantages in comparison with the autoparametric system. First, it generates higher pendulum angular velocities, as shown in Figs. 14(b) and 15(b). Kecik and Boroweic [33] proposed an energy harvesting autoparametric system where they installed an electromagnetic generator at the pendulum pivot point to convert
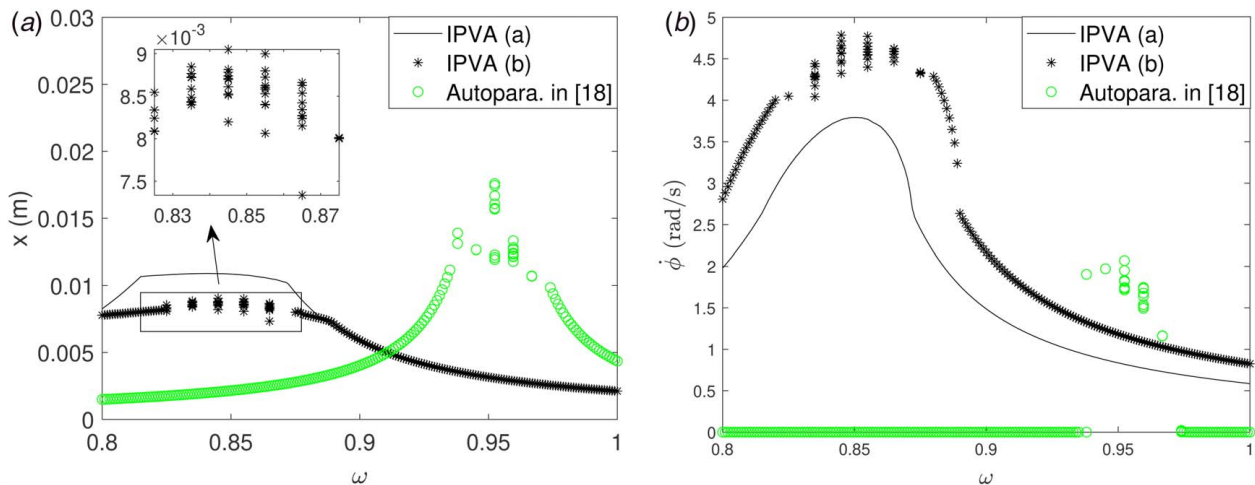

Fig. 14   Comparison of IPVA and autoparametric vibration absorber for a set of parameters: (a) comparison of frequency response of θ for IPVA and autoparametric system with $\eta = 0.4$, $\mu_r = 0.4$, $\xi = 0.005$, and for IPVA $\xi_p = 0.015$, whereas $\xi_a = 0.05$ for autoparametric system and (b) comparison of frequency response of pendulum's velocity for IPVA and autoparametric system with $\eta = 0.4$, $\mu_r = 0.4$, $\xi = 0.005$, and for IPVA $\xi_p = 0.015$, whereas $\xi_a = 0.05$ for autoparametric system
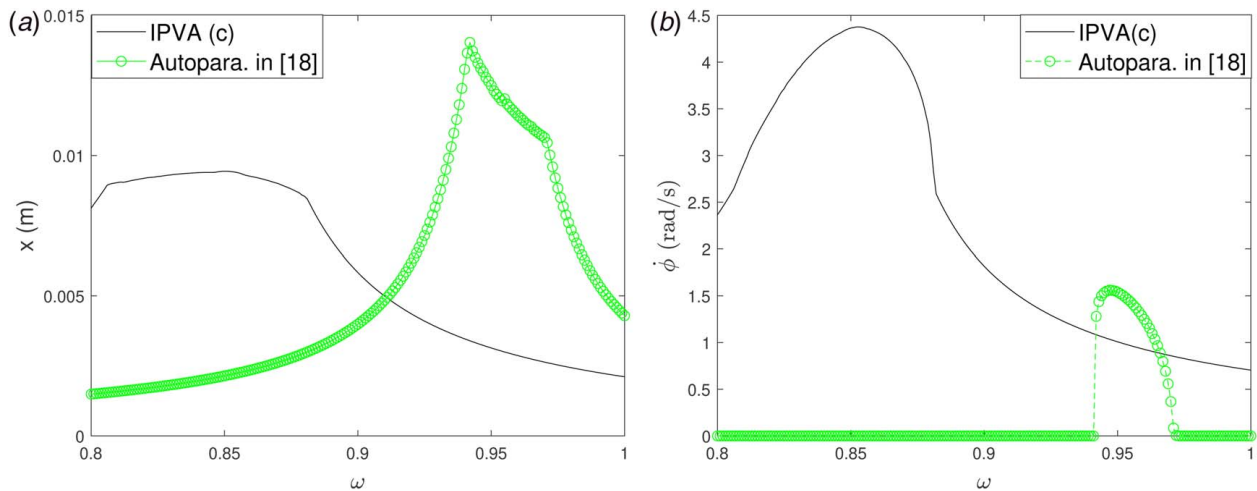
Fig. 15 Comparison of IPVA and autoparametric vibration absorber for a set of parameters: (a) Comparison of frequency response of x for IPVA and autoparametric vibration absorber with $\eta = 0.4$, $\mu_r = 0.4$, $\xi = 0.01$. For IPVA, $\xi_p = 0.015$, and for autoparametric vibration absorber, $\xi_a = 0.05$ and (b) Comparison of velocity of pendulum for IPVA and autoparametric vibration absorber with $\eta = 0.4$, $\mu_r = 0.4$, $\xi = 0.01$. For IPVA, $\xi_p = 0.015$, and for autoparametric vibration absorber, $\xi_a = 0.05$.

the pendulum angular motion into electricity. As the larger angular velocity, the larger electricity can be generated, and the larger angular velocity in the IPVA system may lead to better performance in terms of energy harvesting, which remains to be explored in the future. Second, the IPVA system leads to a more compact design. The largest length in the IPVA system is the sum $R_p + r$ of the carrier radius and pendulum length. IPVA (a) has $R_p + r = 6.69$ cm, which is the maximum among the three. On the contrary, the autoparametric system requires a long pendulum ($l = 12.42$ cm) as it needs this length to tune the natural frequency.

7 Conclusion

This study analyzes the IPVA system proposed in Ref. [34] with a focus on vibration suppression of a linear oscillator subject to single harmonic excitation. It is shown that for a given excitation force magnitude, the pendulum parameters can be chosen such that parametric resonance occurs to the pendulum vibration absorber for a specific range of excitation frequencies. It is also shown that a pitchfork bifurcation and period doubling bifurcation of the pendulum response are necessary and sufficient conditions for the parametric resonance. Furthermore, when parametric resonance occurs, the kinetic energy of the linear oscillator transfers to the pendulum, resulting in vibration suppression of the linear oscillator. A saturation phenomenon similar to autoparametric vibration absorbers and nonlinear vibration absorbers is observed in the IPVA system; that is, the response of the linear oscillator saturates despite the increase in the force magnitude. Meanwhile, the increased energy due to the increase in the force magnitude seems to transfer to the pendulum, resulting in increased pendulum response. Furthermore, the system is compared to the autoparametric vibration absorber. It is shown to outperform the autoparametric vibration absorber in terms of vibration absorption and energy harvesting capabilities.

Acknowledgment

Conflict of Interest

There are no conflicts of interest.

Appendix A: Bifurcation Tracking Algorithm

Algorithm Formulation. A bifurcation tracking algorithm based on Ref. [35] is formulated as follows. First, define a vector function consisting of all the algebraic equations in Eq. (11) as follows:

$$\mathbf{f}(\hat{\mathbf{x}}; \boldsymbol{\lambda}) = \begin{pmatrix} h_0(\hat{\mathbf{x}}; \boldsymbol{\lambda}) \\ h_1^c(\hat{\mathbf{x}}; \boldsymbol{\lambda}) \\ \vdots \\ h_P^c(\hat{\mathbf{x}}; \boldsymbol{\lambda}) \\ h_1^s(\hat{\mathbf{x}}; \boldsymbol{\lambda}) \\ \vdots \\ h_P^s(\hat{\mathbf{x}}; \boldsymbol{\lambda}) \end{pmatrix} \tag{A1}$$

where $\hat{\mathbf{x}}$ is the vector consisting of all the Fourier coefficients in Eq. (11) and $\boldsymbol{\lambda}$ are bifurcation parameters of interest, e.g., $\boldsymbol{\lambda} = \eta$ in Sec. 3.3 and $\boldsymbol{\lambda} = [f, \omega]^T$ in Sec. 3.4. Second, define a scalar function $g(\hat{\mathbf{x}}; \boldsymbol{\lambda})$ that outputs the maximum magnitude of eigenvalues of the fundamental matrix of Eq. (13). A bifurcation point will satisfy the following equations:

$$\mathbf{h}(\hat{\mathbf{x}}; \boldsymbol{\lambda}) = \begin{pmatrix} \mathbf{f}(\hat{\mathbf{x}}; \boldsymbol{\lambda}) \\ g(\hat{\mathbf{x}}; \boldsymbol{\lambda}) - 1 \end{pmatrix} = \mathbf{0} \tag{A2}$$

Now suppose a solution $\hat{\mathbf{x}}_0$ to Eq. (A2) is found for a bifurcation point $\boldsymbol{\lambda} = \boldsymbol{\lambda}_0$, e.g., by numerical integration. To obtain a neighboring bifurcation point, we use an arc length continuation method. Assume that there exists a neighboring solution $\hat{\mathbf{x}}_1 = \hat{\mathbf{x}}_0 + \boldsymbol{\delta}\hat{\mathbf{x}}_0$ for a neighboring bifurcation point $\boldsymbol{\lambda}_1 = \boldsymbol{\lambda}_0 + \boldsymbol{\delta}\boldsymbol{\lambda}_0$ satisfying Eq. (A2) with $\sqrt{\|\boldsymbol{\delta}\hat{\mathbf{x}}_0\|^2 + \|\boldsymbol{\delta}\boldsymbol{\lambda}_0\|^2} << 1$, where $\|.\|$ depicting the ℓ^2 norm.

Imposing the constancy of arc length constraint, we obtain

$$\|\boldsymbol{\delta}\hat{\mathbf{x}}_0\|^2 + \|\boldsymbol{\delta}\boldsymbol{\lambda}_0\|^2 = \|\hat{\mathbf{x}}_1 - \hat{\mathbf{x}}_0\|^2 + \|\boldsymbol{\lambda}_1 - \boldsymbol{\lambda}_0\|^2 = s^2 \tag{A3}$$

where s is sufficiently the small arc length. Therefore, solving Eqs. (A2) and (A3) together will give a neighboring bifurcation point.

Numerical Implementation. The bifurcation tracking algorithm is implemented numerically using Newton–Raphson iterations as follows. Suppose a solution $\hat{\mathbf{x}}_0$ for a bifurcation point $\boldsymbol{\lambda}_0$ is known. Define a new vector function:

$$\mathbf{p}(\hat{\mathbf{x}}, \boldsymbol{\lambda}; \hat{\mathbf{x}}_0, \boldsymbol{\lambda}_0) = \left\{ \begin{array}{c} \mathbf{h}(\hat{\mathbf{x}}; \boldsymbol{\lambda}) \\ \|\hat{\mathbf{x}} - \hat{\mathbf{x}}_0\|^2 + \|\boldsymbol{\lambda} - \boldsymbol{\lambda}_0\|^2 - s^2 \end{array} \right\} \quad \text{(A4)}$$

which needs to equal $\mathbf{0}$ to obtain a neighboring bifurcation point. Suppose two neighboring solutions $\hat{\mathbf{x}}_{k-1}$ and $\hat{\mathbf{x}}_k$ are found for two bifurcation points $\boldsymbol{\lambda}_{k-1}$ and $\boldsymbol{\lambda}_k$, respectively. Denote by $\mathbf{y} = \left[\hat{\mathbf{x}}^T, \boldsymbol{\lambda}^T\right]^T$ the solution to Eq. (A4). A neighboring solution is initially guessed to be

$$\mathbf{y}_{k+1}^g = \mathbf{y}_k + \left(\mathbf{y}_k - \mathbf{y}_{k-1}\right) = 2\mathbf{y}_k - \mathbf{y}_{k-1} \quad \text{(A5)}$$

Next, Eq. (A4) is solved using Newton–Raphson iterations with the initial guess. The correction to the initial guess is given by

$$\mathbf{y}_{k+1}^{(n+1)} = \mathbf{y}_{k+1}^{(n)} - \mathbf{J}^{-1}\mathbf{p}\left(\mathbf{y}_{k+1}^{(n)}; \hat{\mathbf{x}}_k, \boldsymbol{\lambda}_k\right), \quad n = 0, 1, \ldots$$

with $\mathbf{y}_{k+1}^{(0)} = \mathbf{y}_{k+1}^g$ being the initial guess and $\mathbf{J}$ is the Jacobian matrix. To calculate $\mathbf{J}$, we use the forward difference method, i.e., the vth column of $\mathbf{J}$ is expressed as follows:

$$\mathbf{J}(:, v) = \frac{\mathbf{p}\left(\mathbf{y}_{k+1}^{(n)} + \epsilon\mathbf{e}_v; \hat{\mathbf{x}}_k, \boldsymbol{\lambda}_k\right) - \mathbf{p}\left(\mathbf{y}_{k+1}^{(n)}; \hat{\mathbf{x}}_k, \boldsymbol{\lambda}_k\right)}{\epsilon} \quad \text{(A6)}$$

where $\mathbf{e}_v$ is the vth column in the $N \times N$ identity matrix and N being the dimension of $\mathbf{y}$ and $0 < \epsilon \ll 1$. For the calculations in this study, $\epsilon = 10^{-5}$ was taken and the convergence criterion $\|y_{k+1}^{(n+1)} - y_{k+1}^{(n)}\| < 10^{-10}$ was used. Newton–Raphson iterations will give the value of $\mathbf{y}_{k+1}$, this (along with $\mathbf{y}_k$) can be further used to calculate $\mathbf{y}_{k+2}$, thereby tracking the bifurcation points.

Appendix B: Jacobi–Anger Expansion

The Jacobi-Anger formulas used for expansion are as follows [26]:

$$\cos(\phi_0 \sin \psi) = J_0(\phi_0) + 2J_2(\phi_0)\cos(2\psi) + 2J_4(\phi_0)\cos(4\psi) + \ldots, \quad \text{(B1)}$$

$$\sin(\phi_0 \sin \psi) = 2J_1(\phi_0)\sin(\psi) + 2J_3(\phi_0)\sin(3\psi) + 2J_5(\phi_0)\sin(5\psi) + \ldots \quad \text{(B2)}$$

where $J_m(\phi_0)$ is a Bessel function of the first kind of order m. For $\phi_0 = 2.0$ radians (115 deg), $J_4(\phi_0) = 0.034$ and $J_5(\phi_0) = 0.007$. Therefore, only the first two terms are required in the expansion for a good accuracy over a wide range of pendulum oscillations.

References

[1] Smith, M. C., 2020, "The Inerter: A Retrospective," Annu. Rev. Control, Rob., Auton. Syst., **3**, pp. 361–391.

[2] Ikago, K., Saito, K., and Inoue, N., 2012, "Seismic Control of Single-Degree-of-Freedom Structure Using Tuned Viscous Mass Damper," Earthquake Eng. Struct. Dyn., **41**(3), pp. 453–474.

[3] Lazar, I., Neild, S., and Wagg, D., 2014, "Using an Inerter-Based Device for Structural Vibration Suppression," Earthquake Eng. Struct. Dyn., **43**(8), pp. 1129–1147.

[4] Lazar, I., Neild, S., and Wagg, D., 2016, "Vibration Suppression of Cables Using Tuned Inerter Dampers," Eng. Struct., **122**, pp. 62–71.

[5] Qian, F., Luo, Y., Sun, H., Tai, W. C., and Zuo, L., 2019, "Optimal Tuned Inerter Dampers for Performance Enhancement of Vibration Isolation," Eng. Struct., **198**, p. 109464.

[6] Marian, L., and Giaralis, A., 2014, "Optimal Design of a Novel Tuned Mass-Damper–Inerter (TMDI) Passive Vibration Control Configuration for Stochastically Support-Excited Structural Systems," Probabilistic. Eng. Mech., **38**, pp. 156–164.

[7] De Domenico, D., and Ricciardi, G., 2018, "An Enhanced Base Isolation System Equipped With Optimal Tuned Mass Damper Inerter (TMDI)," Earthquake Eng. Struct. Dyn., **47**(5), pp. 1169–1192.

[8] Joubaneh, E. F., and Barry, O. R., 2019, "On the Improvement of Vibration Mitigation and Energy Harvesting Using Electromagnetic Vibration Absorber-Inerter: Exact H2 Optimization," ASME J. Vib. Acoust., **141**(6), p. 061007.

[9] Tai, W.-C., 2020, "Optimum Design of a New Tuned Inerter-Torsional-Mass-Damper Passive Vibration Control for Stochastically Motion-Excited Structures," ASME J. Vib. Acoust., **142**(1), p. 011015.

[10] Qian, F., and Zuo, L., 2021, "Tuned Nonlinear Spring-Inerter-Damper Vibration Absorber for Beam Vibration Reduction Based on the Exact Nonlinear Dynamics Model," J. Sound. Vib., **509**, p. 116246.

[11] Kakou, P., and Barry, O., 2021, "Simultaneous Vibration Reduction and Energy Harvesting of a Nonlinear Oscillator Using a Nonlinear Electromagnetic Vibration Absorber-inerter," Mech. Syst. Signal. Process., **156**, p. 107607.

[12] Yang, J., Jiang, J. Z., and Neild, S. A., 2020, "Dynamic Analysis and Performance Evaluation of Nonlinear Inerter-Based Vibration Isolators," Nonlinear Dyn., **99**, pp. 1823–1839.

[13] Hatwal, H., Mallik, A., and Ghosh, A., 1983, "Forced Nonlinear Oscillations of An Autoparametric System–Part 1: Periodic Responses," ASME J. Appl. Mech., **50**(3), pp. 657–662.

[14] Vyas, A., and Bajaj, A., 2001, "Dynamics of Autoparametric Vibration Absorbers Using Multiple Pendulums," J. Sound. Vib., **246**(1), pp. 115–135.

[15] Bajaj, A., Chang, S., and Johnson, J., 1994, "Amplitude Modulated Dynamics of a Resonantly Excited Autoparametric Two Degree-of-Freedom System," Nonlinear Dyn., **5**(4), pp. 433–457.

[16] Hatwal, H., Mallik, A., and Ghosh, A., 1982, "Non-Linear Vibrations of a Harmonically Excited Autoparametric System," J. Sound. Vib., **81**(2), pp. 153–164.

[17] Song, Y., Sato, H., Iwata, Y., and Komatsuzaki, T., 2003, "The Response of a Dynamic Vibration Absorber System With a Parametrically Excited Pendulum," J. Sound. Vib., **259**(4), pp. 747–759.

[18] Warminski, J., and Kecik, K., 2009, "Instabilities in the Main Parametric Resonance Area of a Mechanical System With a Pendulum," J. Sound. Vib., **322**(3), pp. 612–628.

[19] Yan, Z., and Hajj, M. R., 2015, "Energy Harvesting From an Autoparametric Vibration Absorber," Smart Mater. Struct., **24**(11), p. 115012.

[20] Yan, Z., and Hajj, M. R., 2017, "Nonlinear Performances of an Autoparametric Vibration-Based Piezoelastic Energy Harvester," J. Intell. Mater. Syst. Struct., **28**(2), pp. 254–271.

[21] Kecik, K., 2018, "Assessment of Energy Harvesting and Vibration Mitigation of a Pendulum Dynamic Absorber," Mech. Syst. Signal. Process., **106**, pp. 198–209.

[22] Felix, J. L. P., Balthazar, J. M., Rocha, R. T., Tusset, A. M., and Janzen, F. C., 2018, "On Vibration Mitigation and Energy Harvesting of a Non-Ideal System With Autoparametric Vibration Absorber System," Meccanica, **53**(13), pp. 3177–3188.

[23] Tan, T., Yan, Z., Zou, Y., and Zhang, W., 2019, "Optimal Dual-Functional Design for a Piezoelectric Autoparametric Vibration Absorber," Mech. Syst. Signal. Process., **123**, pp. 513–532.

[24] Sharif-Bakhtiar, M., and Shaw, S., 1992, "Effects of Nonlinearities and Damping on the Dynamic Response of a Centrifugal Pendulum Vibration Absorber," ASME J. Vib. Acoust., **114**(3), pp. 305–311.

[25] Detroux, T., Renson, L., Masset, L., and Kerschen, G., 2015, "The Harmonic Balance Method for Bifurcation Analysis of Large-Scale Nonlinear Mechanical Systems," Comput. Methods. Appl. Mech. Eng., **296**, pp. 18–38.

[26] Newland, D. E., 1964, "Nonlinear Aspects of the Performance of Centrifugal Pendulum Vibration Absorbers," ASME J. Manuf. Sci. Eng., **86**(3), pp. 257–263.

[27] Hamdan, M., and Burton, T., 1993, "On the Steady State Response and Stability of Non-Linear Oscillators Using Harmonic Balance," J. Sound. Vib., **166**(2), pp. 255–266.

[28] Kovacic, I., Rand, R., and Mohamed Sah, S., 2018, "Mathieu's Equation and Its Generalizations: Overview of Stability Charts and Their Features," Appl. Mech. Rev., **70**(2), p. 020802.

[29] Xie, L., Baguet, S., Prabel, B., and Dufour, R., 2017, "Bifurcation Tracking by Harmonic Balance Method for Performance Tuning of Nonlinear Dynamical Systems," Mech. Syst. Signal. Process., **88**, pp. 445–461.

[30] Carroll, T. L., and Pecora, L. M., 1995, Nonlinear Dynamics in Circuits, World Scientific, Singapore.

[31] Gourdon, E., Alexander, N. A., Taylor, C. A., Lamarque, C.-H., and Pernot, S., 2007, "Nonlinear Energy Pumping Under Transient Forcing With Strongly Nonlinear Coupling: Theoretical and Experimental Results," J. Sound. Vib., **300**(3–5), pp. 522–551.

[32] Oueini, S. S., Nayfeh, A. H., and Pratt, J. R., 1998, "A Nonlinear Vibration Absorber for Flexible Structures," Nonlinear Dyn., **15**(3), pp. 259–282.

[33] Kecik, K., and Borowiec, M., 2013, "An Autoparametric Energy Harvester," Eur. Phys. J. Spec. Top., **222**(7), pp. 1597–1605.

[34] Gupta, A., and Tai, W.-C., 2020, "Broadband and Enhanced Energy Harvesting Using Inerter Pendulum Vibration Absorber," International Design Engineering Technical Conferences and Computers and Information in Engineering Conference, Virtual Conference, Aug. 17–19, p. V007T07A007.

[35] Marathe Amol, C. A., 2006, "Asymmetric Mathieu Equations," Proc. R. Soc. A, **462**, pp. 1643–1659.